Comparison of Visual and Acoustic Emission Observations in a Four Point Bending Experiment on Barre Granite

Citation: Li, Bing Qiuyi, and Einstein, Herbert H. "Comparison of Visual and Acoustic Emission Observations in a Four Point Bending Experiment on Barre Granite." Rock Mechanics and Rock Engineering 50, 9 (April 2017): 2277–2296 © 2017 Springer-Verlag

As Published: http://dx.doi.org/10.1007/s00603-017-1233-z

Publisher: Springer-Verlag

Persistent URL: http://hdl.handle.net/1721.1/111129

Version: Author's final manuscript: final author's manuscript post peer review, without publisher's formatting or copy editing

Comparison of Visual and Acoustic Emission Observations in a Four Point Bending Experiment on Barre Granite

Bing Qiuyi Li[1], Herbert H. Einstein[1]

October 2016

[1] Department of Civil and Environmental Engineering, Massachusetts Institute of Technology, Cambridge, MA, 02139, USA.

Tel. +1 617 301 1724. Email: bingqli@mit.edu.

Abstract

We present an experimental study in which a pre-notched specimen of Barre Granite was subjected to fourpoint bending under crack mouth opening displacement (CMOD) control. The experimental observations consisted of load-displacement measurements, acoustic emissions, and photography on a macroscopic (˜cm) as well as microscopic (˜µm) scale. These observations were compared and analysed to better understand process zone development and crack propagation. Load-displacement data showed that the load reaches its maximum at crack initiation, and the machine input work is constant while the crack propagates. AE moment magnitudes between $M_W = -6$ to -10 were observed, and focal mechanisms consisted of both shear and tensile components. During process zone development, AE formed a large cloud of events located near the notch tip and then tended to occur away from the notch tip as the crack propagated. Image analysis at the microscopic scale showed that microcracks formed and coalesced during process zone development; specifically, the microcracks initiated in tension and then propagated as a series of en-echelon cracks. In general, the synthesis of the three observations showed that a wider bulb of activity at lower energy tended to occur during process zone development, while crack propagation tended to be more spatially concentrated and contained higher energy.

Keywords: acoustic emissions (AE), digital image correlation (DIC), rock fracture

1 Introduction

Fracturing and cracking processes in rock are important in geology and in civil-, mining- and petroleum engineering. In the field one can rarely see the fracturing processes and one has to rely on indirect information mostly from seismic signals (Viegas et al., 2015; Vermylen and Zoback, 2011; Collins et al., 2002). In the laboratory, on the other hand, one can visually observe the cracking/fracturing processes and relate them simultaneously to seismic signals in form of acoustic emissions, to deformation, and to the applied load. This has two major benefits: 1. Contributes to basic understanding of the mechanism and 2. Will help in interpreting field observations (Wong and Einstein, 2009; Morgan et al., 2013). In this paper we present an experimental study in which a pre-notched specimen is subjected to fourpoint bending. This is a classic experiment used to observe crack propagation (ASTM C1161, 2013; Pais and Harvey, 2012; Topic et al., 2016). In our study we use this experiment to systematically observe the cracking process with photography and acoustic emissions as well as overall deformation under controlled loading conditions. Similar experiments have been conducted by Alam et al. (2015), Tal et al. (2016), Backers et al. (2005) and Lin et al. (2014) but not in rock with detailed simultaneous monitoring of both the visual observations and acoustic emissions. The purpose of this experiment is to study the relation between visual observations and acoustic emissions using a simple experimental setup in a material with well known properties. This will provide a baseline case study with results one can obtain in close-to-ideal situations. The four point bending geometry ASTM Standard C1161, 2013 was chosen given that it provides a robust method of inducing a tensile stress regime in the bottom half of the specimen, and granite because the material is relatively isotropic, and has been studied extensively both within and outside the MIT research group. The experimental observations consisted of load-displacement measurements, acoustic emissions, and photography on a macro (˜cm) as well as micro (˜µm) scale to observe the behaviour on the specimen scale as well as on the grain scale; the photographic data were evaluated with Digital Image Correlation (DIC). The specific behaviour that we will compare and relate with these three types of observations is the development of the process zone followed by the onset of a crack initiated from a pre-cut notch. The process zone has been observed in rocks by Fortin et al. (2009), Bazant and Kazemi (1990), Olson (2004) and by the MIT rock mechanics group by Morgan et al. (2013), Goncalves da Silva (2016) and Wong and Einstein (2009). It consists of microcracks that can be detected by SEM, optical microscopes, or in some materials by the naked eye through so-called white patching (Morgan et al., 2013; Wong and Einstein, 2009). The microcracks can be tensile, shear or both. As the load increases these microcracks coalesce, propagate as a crack. As will be seen all three types of observations can often but not always be related to the process zone and subsequent crack development. This paper will provide some background on digital image correlation and acoustic emissions in Section 2. The experimental setup is described in Section 3 while the results are presented in Section 4 followed by a summary and conclusions in Section 5.

2 Background

2.1 Digital Image Correlation (DIC)

The Ncorr code (Blaber et al., 2015) is used for all analyses of photographic information. The code performs correlation, based on subset deformation, where for each subset in the reference image a best fit subset is found in the current image. The difference, in the x and y directions between the current and reference subsets are considered to be the u and v displacements. Given that an image is divided into a large number of subsets, a displacement field can then be generated for each current image. The displacements can then be expressed as strain fields ε_{xx}, ε_{xy} and ε_{yy} which can be used to determine the extent of the process zone and the crack. The code has been shown to work well for geotechnical materials (Zhang et al., 2016; Stanier et al., 2015), and a similar approach has been used successfully on the micro-scale in marble (Tal et al., 2016). For the purposes of this paper ε_{xx} is considered as opening or tensile strain, given that it corresponds to the primary tensile stress induced by the four point bending geometry. Similarly, ε_{xy} is considered to be the shear strain given that it is oriented 45 degrees to the primary tensile stress field, and is required in addition to ε_{xx} in order to fully understand the Mohr's strain circle. Note that a positive ε_{xy} describes a motion where the "top" half of the fracture moves "leftwards" while a negative ε_{xy} describes the reverse situation. The full strain state is considered because this and other studies (Morgan et al. 2013, Gonçalves 2016) have noted en-echelon cracking even in a generally tensile stress state.

One of the main limitations of applying DIC to a material that develops a crack is that generally, the displacement and strain calculations cannot account for the discontinuities. Blaber et al., (2015) provide a solution to this by allowing the subset to be truncated at the crack. However, this method requires the crack geometry to be precisely known. In the experimental setup, the crack opening was small enough such that the overlying paint did not separate, and so this solution could not be applied since the exact crack geometry could not be identified. As a result, areas immediately near the crack may not describe the strain experienced by the material if the pixels are within the zone of influence of a crack. To mitigate this, we have chosen the subset radius to be as small as possible to minimise the pixels over which the discontinuity affects the results. The drawback of the small subset radius is that it tends to increase the noise observed in the DIC results. A quantitative treatment of this source of error is presented in Section 2.1.1.

Nevertheless we present most of our visually observed data and interpretations in the form of strains as opposed to displacements since it more clearly illustrates the extent and nature of the process zone both at the micro- and macro- scale. This is also justified given that, as will be shown in Section 4.4.1, there is a gradual transition from the process zone to the existence of a crack.

2.1.1 DIC noise quantification

In order to understand the level of background noise in the DIC method as applied to the photos, two images captured two seconds apart during the elastic deformation stage were chosen since the amount of displacement is minimal and it is assumed that the majority of the calculated displacement can be attributed to noise. DIC was applied between these two images, and the opening displacement is shown in Figure 1. The ε_{xx}, which was calculated from the displacements, is shown in Figure 2. These are shown at subset radii of 15, 30 and 60 pixels, where 15 was the radius used in this study. The larger radii produce data that are less noisy since they are averaged over a wider area.

[Figure 1]

[Figure 2]

Figure 1 shows that for the displacement data, the noise in general increases as the subset radius shrinks. Specifically, it is observed that much of the noise occurs in the form of zones of zero displacement, which is particularly notable for the data calculated from a radius of 15 pixels. This may be attributed to the speckle pattern, which due to its random nature contains larger areas that are entirely white or black, and so using a smaller radius causes the displacement calculated from these monochromatic zones to be zero. However, it can be seen that overall the magnitudes and trends in the displacement are consistent between the 15 pixel radius used in this study and the larger radii. In terms of the strain shown in Figure 2, it appears that a doubling of the radius results in approximately three times the standard deviation in the strain, which was true for the increase from 15 to 30 pixels, and 30 to 60 pixels. This implies that the error decreases linearly from a 15 pixel radius to a 60 pixel radius, and so there is no optimum point at which a larger radius provides marginal benefits to noise reduction. As a result, the smallest radius of 15 pixels was chosen since this minimises the area over which the crack discontinuity affects the displacement and strain data. As shown in Figure 3, the noise is still small enough such that it does not significantly inhibit the ability to discern process zone features and extent. We suggest that areas within this 15 pixel radius, along with areas exhibiting strains above a threshold opening strain of 3%, as will be discussed in Section 4.5.3, are likely those affected by the discontinuity of the crack. However, it is important to note that the focus of this paper is on the shape, extent, and features of the process zone as opposed to the specific magnitude of the strains.

A similar quantification of noise is shown for the micro-DIC in Figure 4, where we chose the smallest subset radius from which displacement could be reliably calculated. The noise is larger in the micro-DIC than the macro-DIC due to the 25 μm spacing on the mesh, which has a larger spacing between features than the optimal 3x3 pixel/speckle size in the current state of practice. This regular mesh configuration is less accurate than speckling since the pattern is not unique. It was not possible to use a smaller mesh as they are very easy to tear as the spacing becomes smaller.

[Figure 3]

[Figure 4]

2.2 Acoustic Emissions (AE)

Acoustic emissions are elastic waves that are emitted from most materials caused by cracking or other dislocations, and are effectively synonymous to microseismicity. Hence, the data presented in this paper are analysed as done for seismic signals. Regarding arrival time picking, it was found that in some cases, the fixed 3 ms duration of a recorded waveform contained multiple emissions, and so a modification was made to the Aikake Information Criterion (AIC) (Maeda, 1985), where the AIC is calculated in small (~0.1 ms) moving time windows to facilitate multiple detections per 3 ms waveform. Locations are determined from the minimisation of residuals as outlined in Shearer (2009) using a constant velocity model and optimised by the fminsearch function in MATLAB. Moment tensor inversion and decomposition are performed according to the 2D implementation of the SiGMA (Grosse and Ohtsu, 2008) algorithm, where events with a double couple (DC) component greater than 40% are considered shear, and tensile otherwise. We use the 2D case given the thin specimen geometry, where we can assume a plane stress condition which results in a 2D stress field. While it is true that the grains in the granite are not 2D in nature, Figure 14 indicates that the majority of the crack is reasonably planar. One of the goals of the paper is to compare AE to the 2D DIC analysis, and so we are most interested in the in-plane direction. The magnitudes of AE events were calibrated to the absolute moment magnitude (M_W) values using the scheme outlined in McLaskey et al. (2015) that will be further described in Section 3.

3 Experimental Setup

3.1 Physical Setup

The specimen (dimensions 241.3 x 51 x 25.4 mm) was set up as shown in Figure 5. The material was Barre Granite from Vermont. The top loading platens were not spaced as per ASTM standards, to accommodate the dimensions of our loading machine, which are acceptable given that the absolute value of the ultimate load was not of interest. The used spacing was adequate to generate a repeatable stable stress condition. An extensometer was attached to the notch opening, and the experiment was operated under Crack Mouth Opening Displacement (CMOD) control at a constant rate of 0.0127 mm/min (see Figure 9b).

[Figure 5]

3.2 AE Setup

The experiment was instrumented with seven PAC (Physical Acoustics Corporation) Micro30S sensors, attached with 0.002” acrylic double sided tape, at 40 dB amplification. The eighth sensor was a 28 dB amplified Glaser-type sensor coupled with honey since its contact is a conical tip and so cannot be attached with tape. This sensor was attached for calibration purposes and worked as well as the PAC sensors for localisation and moment tensor inversion. All sensors were connected to PCI-2 data acquisition cards from PAC at 5 MHz, with 35 dB trigger for the PAC sensors and 50 dB for the Glaser-type sensor because of different noise floors. The acquisition setup is designed to record semi-continuously if necessary, with approximately 80% uptime. The AE signals are recorded in terms of voltages over time, and need to be calibrated to a physical quantity for comparison to the load-displacement and strain observations. In this study, we use an empirical calibration method developed by McLaskey et al. (2015), which relates an AE event to moment magnitude (M_w), a parameter commonly used in seismology that describes the total energy transformed during an earthquake (Shearer, 2009). The basis of the method is that the entire system (rock specimen, sensors, preamplifiers, acquisition system) is grouped into a single experimental transfer function that describes how a source (for example, the contact force of a ball drop) is transformed into a recorded electrical signal. This transfer function is determined by dropping a steel ball onto the rock specimen and recording the waveform, which is then divided by its theoretical Herztian contact function in the frequency domain. The transfer function for our experiment is shown as the blue curve in Figure 6a for a 1.58 mm steel ball using the same notation as McLaskey et al. (2015). Then, the ratio is determined between this transfer function and that of an AE event, and this ratio is taken to be proportional to its moment magnitude. This calibration was performed for 3 AE events (shown as the red, yellow and purple curves in Figure 6a with different first motion amplitudes to capture a range of behaviours, so that the relation between the voltage and M_w can be generalised for the entire catalogue of AE events. In this case, the calculated M_w values were -9.78, -8.45 and -6.91, and it was found that there is a loglinear relation between an event's M_w and its first motion amplitude (Figure 6b). This relation was assumed to be correct for the entire experiment since the 3 selected AE events span the range of amplitudes seen in the experiment. Thus, it was applied to the first motion amplitude of all events to calculate its respective M_w. The results are plotted as a cumulative histogram, traditionally known as a magnitude-frequency distribution plot (Gutenberg and Richter, 1954), shown in Figure 7. It can be seen that the events in the experiment span from M_w = -9.8 to -6.25, supporting the original notion that the three hand-picked events cover the range of events recorded during the experiment.

[Figure 6]

[Figure 7]

As seen in Figure 7, the events from the experiment roughly follow the expected quasi-linear relation between magnitude and frequency distribution, with a slight increase in b-value towards the higher magnitudes. The M_w values range from -6 to -10, which overlap with but are on average smaller than other experiments in granite such as those by Yoshimitsu et al. (2014), where the events tend to cluster between M_w of -5 to -7. The larger AE events also lie in the same range as described in McLaskey et al. (2015), who calibrated two AE events to -6.4 and -7.2. As a basis for comparison, the total M_0 (moment magnitude) for all events was calculated to be 0.74 [Nm = J], which can be used in the analysis described in Section 4.

3.3 Camera Setup

The experiment was instrumented with two cameras. On the front face, a Canon 6D was used with a Tokina 100mm f/2.8 ATX M100 lens at a distance of around 40 cm such that the field of view was approximately 7.5 cm x 10 cm. On the back face, we used a Canon SL1 with a 65mm MP-E macro lens at 5X such that the field of view was approximately 2.95 mm x 3.93 mm. For surface preparation, the side facing the front camera was painted with a white acrylic paint background with black paint sputtered at around 0.1 to 1 mm speckle size. The back side was painted with the same white acrylic background paint, then polished to 10 μm grit with alumina powder and sputtered with carbon black on a 1000 Nickel mesh to create a grid pattern with approximately 25 μm spacing. Figure 8 shows photos of the prepared specimen. For simplicity, analyses of images from the front camera will be referred to as ”macro-images” or ”macro-DIC” and likewise back camera images and analyses as ”micro-images” and ”micro-DIC”. The macro-DIC is performed with reference to time 143 s, and the micro-DIC is referenced to time 147 s.

[Figure 8]

3.4 Repeatability

To ensure that the results are consistent, two repeats (i.e. three tests in total) of the same experiment were performed. The load-displacement graphs are shown in Figure 9a. The drop in load close to the end of the elastic region are due to refocusing of the cameras. During the pause the position of the crosshead was held constant, but the machine software is such that no data are acquired when the experiment was paused. When the machine is restarted the load drops for the duration of 2-4 data points (0.01 s data acquisition interval). This is unfortunately unavoidable since the specimen expands in the depth dimension due to the Poisson effect such that the micro-camera requires refocusing at the end of the initial loading phase. This must be done manually since autofocus in unreliable in this setup.

The peak loads and crosshead displacement are similar for the three experiments; the elastic phase (linear region of the force-displacement plot) has slightly different slopes while the plastic phase (post-linear region of the force-displacement plot) follows a different path in each experiment. These differences may be attributed to heterogeneities within the granite specimens. Note that all three experiments transition from the linear region at approximately 2.3 x 10^{-4} m of crosshead displacement and appear to show some stick-slip behaviour during the plastic and cracking phase in that the load is constant for a period of time before increasing and decreasing rapidly. Since the load-displacement behaviour was reasonably similar and the AE and DIC trends were similar in all experiments, the discussion of results will be focused on the first experiment.

[Figure 9]

4 Results

4.1 Overview

As mentioned in the introduction, the granite specimen was subjected to four point bending to generate tensile stresses, which result in the formation of a process zone consisting of microcracks, which then coalesce and develop into a crack. This process was forced to occur slowly under crack mouth opening control, such that different observation methods could be used to describe the cracking process. Specifically, these observations are 1) Load-displacement behaviour, 2) Strains observed on the surface of the specimen and interpreted by DIC and 3) Acoustic emissions. The results section will first present the load-displacement data, which is then compared to the corresponding visual and acoustic emissions data.

4.2 Load-displacement behaviour

Figure 10 shows the load-displacement data for the entire experiment, and it can be seen in Figure 10b that the loading curve consists of three main stages: an initial linear phase (’a’), followed by a non-linear period of increasing load (’b’), and finally a monotonically decreasing load while the crosshead is held constant (’c’). The load-displacement curve can be integrated to produce the machine input energy, as shown in Figure 11. Note that the maximum machine energy input is around 0.7 J, which is similar to the total M_0 that was calculated in the previous section.

[Figure 10]

[Figure 11]

Figures 10 and 11 indicate three distinct stages which can be interpreted as ’a’ elastic deformation, ’b’ process zone development and ’c’ crack initiation and propagation, where crack initiation is considered to be the first time a new traction free surface is created, and crack propagation refers to the continued creation of such traction free surfaces. Both the load-displacement and energy-time data support this interpretation, which also correspond to the stages outlined in Eberhardt et al. (1999), although we have chosen to interpret their crack initiation and stable crack growth stage as the development of the process zone. These stages are now used as the basis of comparison for the visual and AE observations. Note that although a crack initiates and propagates in stage ‘c’, a process zone continues to develop ahead of the propagating crack tip.

4.3 General comparison of strain and AE observations

These comparisons will first be done for the entire experiment to evaluate general trends in behaviour, and then specifically for stages ’b’ and ’c’ of the load-displacement curve.

4.3.1 Strain observations

Figure 12 shows the macro-DIC opening strain at key points in time corresponding to the load-displacement curve (Fig. 10a), to determine the extent of damage that can be visually observed on the specimen. Note, as described in Section 2.1, that some of the strains are calculated across discontinuities.

[Figure 12]

Figure 12 shows that at time 209 s, very little deformation can be seen given the noise threshold of the DIC method. This is to be expected as the load-displacement curve indicates that the behaviour is elastic until this point, and that the displacement is quite small. However by 259 s, there is a zone of significant opening strain extending around 2 mm from the notch tip. This again is consistent with the load curve, which shows a small amount of non-linear deformation by this time. By 309 s there is a large, 2-3 mm wide zone of deformation extending around 7 mm ahead of the notch tip. This zone of deformation then decreases in size by 549 s, likely caused by unloading of the rock at that location since the crack tip and its corresponding process zone move upwards as the crack propagates.

4.3.2 AE observations

Figure 13a shows the location of AE events over the course of the experiment. There is significant scatter in the horizontal direction even with the imposed 1 mm accuracy for localisation, which implies that the approximately 10 mm wide scatter of event locations can be attributed to the formation of a process zone (Wong and Einstein, 2009) as cracking propagates through the specimen. This is significantly wider than the 2 mm process zone observed in the DIC. An explanation is that the AE may be sensitive to smaller perturbations. As expected, the AE locations shift upward as cracking propagates (See time scale in Figure 13a), but again there seems to be significant scatter in the vertical direction, highlighting the stochastic nature of AE events stemming from heterogeneities in the crystalline rock specimen. It is also notable that at around location (x = 120 mm, y = 23 mm) there is a small zone of approximately 1 mm in diameter that is lacking in AE events, indicating that there may be a particularly high strength mineral grain at that location.

[Figure 13]

Figure 13b shows the largest AE events, coloured by their magnitude. There appears to be wider scatter of locations near the notch tip, which may be due to a wider process zone prior to crack initiation and is consistent with Figure 12, which showed a large process zone near the notch tip. Overall, the large events shown in Figure 13b seem to occur closer to the crack path than Figure 13a, which shows all the events. This suggests that the larger events are more critical to the creation of the crack itself, whereas smaller events are more likely to be related to the continued development of the process zone ahead of the propagating crack tip. Interestingly, there appears to be a significant semicircular pattern to the event locations again at around (x = 120 mm, y = 23 mm), suggesting that the larger AE events may be preferentially occurring at grain boundaries. This happens at other locations that are circled in Figure 13b, and is supported by visual inspection which showed, for example, that there was a large quartz grain (Fig. 14) approximately 10 mm from the notch tip. Overall, it appears that the AE locations correspond to the strain maps, both showing a larger scatter around the notch tip that may be associated with the initial process zone.

[Figure 14]

More information can be gained by considering details of the AE evolution over time and space. This is done in Figure 15, which shows the magnitude-frequency distribution of AE events, which shows the proportion of large compared to small events. Different curves show the b-value at various times and distance from the notch tip.

[Figure 15]

Figure 15a shows that the development of the process zone, which occurs between 200 and 300 s, contains the fewest and lowest magnitude events. This is consistent with the behaviour observed in the energy-time curve, which suggests that crack propagation is more energetic than process zone development. Interestingly, this time period has a shallower slope than the 300 - 400 s and 500 - 600 s period, indicating that small events comprise a lower proportion of events during this time. As expected, the time between 400 and 500 s contains the most and highest magnitude events, which is consistent since this is the period of greatest machine work. Figure 15b shows the b-value for events grouped according to their distance from the original notch tip. We can see that the highest concentration of events is at 5-15 mm from the tip, followed by those at 15-25 mm, then by those right at the notch tip. The 5-10 mm grouping has a similar total number of events as the 10-15 mm grouping, but the 5-10 mm grouping has more large magnitude events, indicating that crack initiation may be associated with the largest events given that this grouping is quite close to the notch tip. This is supported by the 0-5 mm grouping, which has a small total number of events but also has a greater proportion of large magnitude events compared to the 10-25 mm groupings. In fact, one may conclude that the slope becomes steeper with distance from the notch tip, i.e. smaller events dominate with increasing distance from the notch tip. Figure 16 shows the AE hit rate for the experiment, which increases linearly until approximately 340 s and maintains a steady rate until approximately 550 s, where it begins to slow down. This pattern appears to match well with the loading machine work shown in Figure 11, which is constant between 350 s and 550 s.

[Figure 16]

There also appears to be more variability in the hit rate between 400 s and 600 s than in the previous 200 seconds, in that there are multiple large increases in activity even though the rate remains constant on average. This can be explained by stick-slip behaviour or small-scale heterogeneities of the material resulting in more emissions produced when the crack moves through a higher strength material. However, this is difficult to verify given that one cannot determine the extent of the crack at depth over time. Overall, it appears that the load-displacement, strain (DIC), and AE observations are reasonably consistent. Specifically, all three observations show that stage b, which consists of process zone development, is associated with a wider bulb of lower energy activity near the notch tip. This is markedly different from stage c, which consists of crack propagation and appears to be higher energy and less spatially dispersed horizontally. For this reason, the two stages are now discussed separately in more detail.

4.4 209 s to 309 s: Process zone development

Between 209 s and 309 s (See stage b in Fig. 10), the machine load is monotonically increasing and the deformation is non-linear; the machine is constantly putting work into the system (Fig. 11).

4.4.1 Strain observations

Figure 17 shows the ε_{xx} and ε_{xy} strains from the micro-DIC at three different points in time. At 253 s, the microcracks have propagated to around 0.6 mm from the notch tip, which is a very small distance compared to the AE events (Figure 13), which reach up to 15 mm from the notch tip. One can also note that the first 0.5 mm of the microcracks initiate in tension given that at 253 s ε_{xx} shows significant opening strain but very little ε_{xy} contribution (zone a in Figure 17). After the initial 0.5 mm, it appears that the microcracks propagate as a series of en-echelon cracks (zone b in Fig. 17). These en-echelon microcracks occur at approximately 45 degrees to the tensile stress direction as expected, but there appears to be a preference for the SW-NE orientation, a trend that was also observed in the two repeat experiments and may be due to a bias in the loading machine. It is also interesting to note that at approximately 250 s the macro-DIC (Figure 12) indicates a zone of increased strain that extends 2 mm from the notch tip, but the same time frame for the micro-DIC only indicates microcracking up to around 0.5 mm from the tip, and even at 275 s only extends approximately 1 mm from the notch tip. The much smaller extent of the strain-intense areas in the micro-DIC may be due to the small 3 mm field of view, such that general changes in strain seen in the macro-DIC fall into the background noise of the strain plots seen in Figure 17. As a result, the micro-DIC only highlights what may be referred to as linear white patching (Morgan et al., 2013; Wong and Einstein, 2009) i.e. the process zone visible by eye as a white line.

[Figure 17]

4.4.2 AE observations

In terms of the AE data, the event locations shown in Figure 18 indicate that majority of events are dispersed, and cluster in an area around 10 mm from the tip of the notch. A vertical linear series of events appears to occur near the notch tip at around 250 s (Cluster a), and another linear cluster at around 270 s (Cluster b), indicating that there may have been concentrated microcracking at these locations. A look at the source mechanisms and magnitudes shown in Figure 19 indicates that the tensile events are much fewer and appear to occur somewhat away from the notch tip when compared to the shear events, which form the majority of the cluster immediately at the notch tip. As expected, the tensile microcracks are oriented along the orientation of the eventual crack, but the shear events appear to have a wide distribution of orientations. The magnitudes appear mostly to be quite small in this time period. Interestingly, the tensile events do not show the initial tensile portion noted as ’a’ in Figure 17. This may be due to the small size of this tensile feature, such that it is not captured by the AE which averages behaviour across the specimen. Unfortunately, attempts to directly map the AE locations to observations in the micro-DIC were not successful, given that the location accuracy of the AE at 1 mm is considerably larger than the resolution of the micro-DIC at around 25 μm.

[Figure 18]

[Figure 19]

4.4.3 Comparison of AE and visual data between 209 s and 309 s

To relate the DIC and AE data, Figure 21 shows the evolution of the strains over time at specified query points. At point 1 (query points are shown in Figure 20), corresponding to the tensile zone noted previously, the rock has higher opening strain than elsewhere; it also begins to significantly open at around 260 s, approximately 10 seconds before the rock at other query points. It is also interesting to note that the remainder of the query points, though they are separated in space, all show very similar behaviour in that they begin to open around 270 s, albeit at slightly different rates. Given that a qualitative observation of Figure 17 shows that strains develop as early as approximately

250 s, this indicates that the early strains are quite small such that they fall within the noise band of the DIC analysis (the standard variability of strains seen between 240-260 s). As expected, ε_{xy} exhibits both positive and negative strains corresponding to the two possible orientations of the en-echelon cracks. However, it is notable that the positive (SW-NE) strains are approximately five times larger than the negative strains, which agrees with the general preference for the SW-NE direction noted earlier. There also appears to be some grouping of shear behaviour for the rock at separate locations, for example the behaviour at point 1 is similar to point 3; likewise points 4 and 6, 5 and 7 show similarity to each other. These points appear to develop strain at approximately the same rate, possibly suggesting that separate sections of the en-echelon cracks may be developing simultaneously. The overall strain observations indicate that microcrack initiation begins around 260 s, which corresponds to the middle of stage "b" on the load-time graph shown in Figure 10. The AE hit rate fluctuates significantly over the period of analysis, and one may argue the times of high AE activity are related to local minima or maxima in query point 1 of Figure 21a. However this relation would be tenuous at best since the DIC only samples the surface of the specimen, while AE data pertain to the entirety of the specimen.

[Figure 20]

[Figure 21]

4.5 309 s to the end of the experiment: Crack propagation

Post-load-peak behaviour (stage c in Figure 10) generally consists of the continued growth of the crack, and is characterised by the further development of en-echelon cracks as shown in Figure 22.

4.5.1 Strain observations

As seen in Figure 22, the process zone appears to grow approximately linearly over time, as expected from the nature of CMOD control. It is also evident from the ε_{xy} plots that alternating red and blue areas indicate alternate sections of en-echelon cracks.

[Figure 22]

Query points (Figure 23c) can again be considered for the DIC analysis, of which the strains over time are plotted as shown in Figures 23a and 23b. There appear to be some anomalies at later times for query points 1, 2 and 3 due to significant opening of the discontinuity as described in Section 2.1.1, but overall the analysis shows a somewhat linear development of strain over time, with the query points furthest from the notch tip being the last to exhibit strains.

[Figure 23]

4.5.2 AE observations

The AE events follow a general pattern with events moving upward with time as the crack propagates. However, there is significant scatter in this trend, both in time and space. The tensile microcracks are again oriented primarily vertically as expected since the crack propagates upwards, with the highest magnitude events occurring closest to the center of the cluster. The shear events are more numerous, and also appear more scattered than the tensile events, possibly due to shear occurring at multiple grain boundaries near the propagating crack while tensile events only occur at the crack itself. However, the magnitudes do not appear to differ significantly between the mechanisms.

[Figure 24]

4.5.3 Comparison of AE and visual observations

Similar to the previous section, it is important to compare the strains from image analysis with the AE results for this time period. The extent of the process zone and the crack can be estimated from the ε_{xx} contours such as those shown in Figure 22. These were determined by considering a large number of query points located along an iso-displacement contour in the opening displacement plot (Figure 25a), which best represented the location of the crack based on the ε_{xx} and ε_{xy} plots. The ε_{xx} at these points were then evaluated as a function of time and distance from the notch tip as shown in Figure 25b. The process zone was considered to have reached a query point if the strain exceeded the noise level at that point, which varied slightly between points but is generally less than 0.003. To determine the crack extent, the following was done: the load-displacement curve indicates that the crack initiates at approximately 309 s into the experiment. With this a strain value was calibrated such that the strain along any query point first exceeds this critical value at approximately 309 s. This value was found to be 0.03, or 3% in this experiment, as shown in Figure 25b. Note that although the crack initiation appears to be a distinct point in the load-displacement curve, the AE and DIC data do not suggest such a dramatic transition. As a matter of fact there is a gradual transition from the process zone to a fully cracked surface as multiple bonds with variable strength must be broken to create the free surface. The extent of the process zone and the crack can then be plotted alongside the distance from the notch tip of all AE events, as shown in Figure 26.

[Figure 25]

[Figure 26]

In Figure 26, the red line shows the furthest extent of the process zone that can be seen by the DIC. Similarly, the brown line is the best estimate of the distance of the crack tip from the original notch tip. As a result, the area between the two lines represents the range of the process zone length. Figure 26a shows that the highest spatio-temporal concentration of the AE events fall within the zone bounded by the two lines, particularly the high amplitude events (Figure 26b), but that there are some exceptions. The AE locations beyond the process zone determined by the DIC may again suggest that the AE event locations are more sensitive to small strains than the DIC. There are also AE events closer to the notch tip than the crack extent, but these may be explained by noting that Figure 26b shows that many of the events near to the notch tip seem to be high in shear. This may be occurring due to shearing along already open en-echelon cracks.

5 Summary and conclusions

Process zone development and crack propagation have been observed on a pre-notched four point bending experiment on granite. The experiment consisted of observations of load-displacement, strains on the specimen, and acoustic emissions, which were analysed and compared. The main results are summarised as follows:

- Calibration of AE events to moment magnitudes indicate that the events vary from $M_w = -6$ to -10, with a total transformed energy of around 0.7 J.

- Load-displacement and corresponding energy-time data indicates three main stages of rock behaviour: ’a’ Elastic deformation, ’b’ formation of a process zone, and ’c’ crack propagation. These stages appear to be relatively accurately for describing changes in AE and DIC behaviour.
- Strain and AE observations over the course of the experiment show that during stage ’b’, a wide bulb of lower energy activity develops around the tip of the pre-cut notch. During stage ’c’, more energy is released and consumed in the propagation of the crack, together with less horizontal scatter of the AE event locations.
- During stage ’b’, the formation of microcracks appears to initiate in tension, and then continue to appear as a series of en-echelon cracks in shear, which is supported by the focal mechanisms of AE events. The extent of these microcracks are on the sub-mm scale for this experiment, and as such are beyond the spatial resolution of acoustic emissions and macro-DIC, each of which show the process zone developing as a semi-elliptical bulb of strain.
- A consideration of the evolution of strains over time and space and the load-displacement data showed that at approximately 3% strain the process zone transitions into the crack front.
- An estimate of the extent of the process zone and the crack itself from DIC data compared well with the extent of AE locations, although the AE cloud tended to be slightly larger than the DIC process zone.

We can therefore conclude that the simultaneous observation of load-displacement, strain, and acoustic emissions and the relations between them provide a reasonably holistic picture of the development of the process zone and crack propagation. This is important as it will aid in the interpretation of other laboratory results and eventually field observations, where usually only one of these data types is available.

Acknowledgements

The research presented in this paper was supported by TOTAL SA. The authors would like to express their sincere gratitude for this support. We would also like to thank Professors Brian Evans, John Germaine and German Prieto, and Dr. Ulrich Mok for the insights and suggestions.

Bibliography

Alam, S., Loukili, A., Grondin, F., and Roziere, E. (2015). Use of the digital image correlation and acoustic emission technique to study the effect of structural size on cracking of reinforced concrete. Engineering Fracture Mechanics, pages 17–31.

ASTM C1161 (2013). Standard Test Method for Flexural Strength of Advanced Ceramics at Ambient Temperature. American Society for Testing and Materials (ASTM).

Backers, T., Stanchits, S., and Dresen, G. (2005). Tensile fracture propagation and acoustic emission activity in sandstone: The effect of loading rate. International Journal of Rock Mechanics and Mining Sciences, 42:1094–1101.

Bazant, Z. and Kazemi, M. (1990). Determination of fracture energy, process zone length and brittleness number from size effect, with application to rock and concrete. International Journal of Fracture, pages 111–131.

Blaber, J., Adair, B., and A., A. (2015). Ncorr: Open-source 2d digital image correlation matlab software. Experimental Mechanics. Collins, D. S., Pettitt, W. S., and Young, R. P. (2002). High-resolution mechanics of a microearthquake sequence. Pure and Applied Geophysics, pages 197–219.

Eberhardt, E., Stead, D., and Stimpson, B. (1999). Quantifying progressive pre-peak brittle fracture damage in rock during uniaxial compression. International Journal of Rock Mechanics and Mining Sciences, 36:361–380.

Fortin, J., Stanchits, S., Dresen, G., and Gueguen, Y. (2009). Acoustic emissions monitoring during inelastic deformation of porous sandstone: Comparison of three modes of deformation. Pure and Applied Geophysics, pages 823–841.

Goncalves da Silva, B. M. (2016). Fracturing processes and induced seismicity due to the hydraulic fracturing of rocks. PhD thesis, Massachusetts Institute of Technology.

Grosse, C. U. and Ohtsu, M. (2008). Acoustic Emission Testing. Springer.

Gutenberg, B. and Richter, C. (1954). Seismicity of the Earth. Princeton Press, 2 edition.

Lin, Q., Huina, Y., Biolzi, L., and Labuz, J. F. (2014). Opening and mixed mode fracture processes in a quasi-brittle material via digital imaging. Engineering Fracture Mechanics, pages 176–193.

Ludovico-Marques, M., Chastre, C., and Vasconcelos, G. (2012). Modelling the compressive mechanical behaviour of granite and sandstone historical building stones. Construction and Building Materials, pages 372–381.

Maeda, N. (1985). A method for reading and checking phase times in autoprocessing system of seismic wave data. Journal of the Seismological Society of Japan, pages 365–379.

McLaskey, G. C., Lockner, D. A., Kilgore, B. D., and Beeler, N. M. (2015). A robust calibration technique for acoustic emission systems based on momentum transfer from a ball drop. Bulletin of the Seismological Society of America, pages 257–271.

Morgan, S., Johnson, C., and Einstein, H. (2013). Cracking processes in barre granite: fracture process zones and crack coalescence. International Journal of Fracture, pages 177–204.

Olson, J. E. (2004). Predicting fracture swarms—the influence of subcritical crack growth and the crack-tip process zone on joint spacing in rock. Geological Society, London, Special Publications, pages 73–88.

Pais, J. C. and Harvey, J. T. (2012). Four point bending. CRC Press.

Shearer, P. M. (2009). Introduction to Seismology. Cambridge University Press.

Stanier, S., Blaber, J., Take,W., and White, D. (2015). Improved image-based deformation measurement for geotechnical applications. pages 727–739.

Tal, Y., Evans, B., and Mok, U. (2016). Direct observations of damage during unconfined brittle failure of carrara marble. Journal of Geophysical Research: Solid Earth, 121:1584–1609.

Topic, J., Bartos, J., Kopecky, L., Seps, K., Pros, Z., and Trejbal, J. (2016). Cement composite reinforced with synthetic fibers: Comparison of three-point and four-point bending test results. Applied Mechanics and Materials, pages 332–335.

Vermylen, J. and Zoback, M. D. (2011). Hydraulic fracturing, microseismic magnitudes, and stress evolution in the barnett shale. In SPE Hydraulic Fracturing Technology Conference, The Woodlands, Texas, USA.

Viegas, G., Urbancic, T., Baig, A., and von Lunen, E. (2015). Rupture dynamics and source scaling relations of microseismic hydraulic fractures in shale reservoirs. In Proceedings of the 13th International ISRM Congress 2015.

Wong, L. and Einstein, H. (2009). Crack coalescence in molded gypsum and carrara marble: part 1 - macroscopic observations and interpretation. Rock mechanics and Rock Engineering, pages 475–511.

Yoshimitsu, N., Kawakata, H., and Takahashi, N. (2014). Magnitude -7 level earthquakes: A new lower limitof self-similarity in seismic scaling relationships. Geophysical Research Letters, pages 4495–4502.

Zhang, J., Peng, W., Liu, F., Zhang, H., and Li, Z. (2016). Monitoring rock failure processes using the hilbert–huang transform of acoustic emission signals. pages 427–442.

Figures

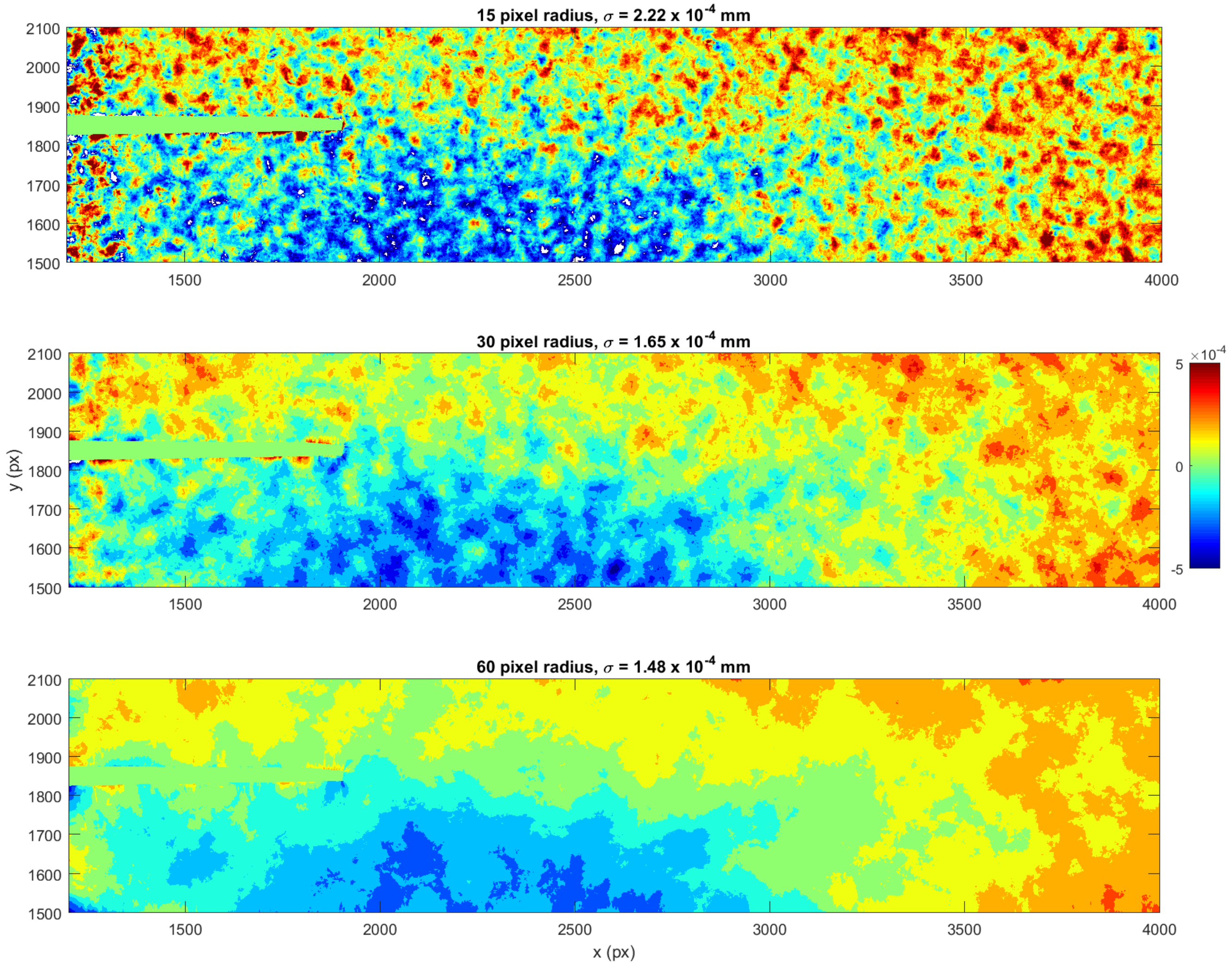

{v_close_calib.eps}

Figure 1: Opening displacement (mm) for images taken 2 seconds apart using different subset radii. Standard deviation of the displacement map is given in each figure heading.

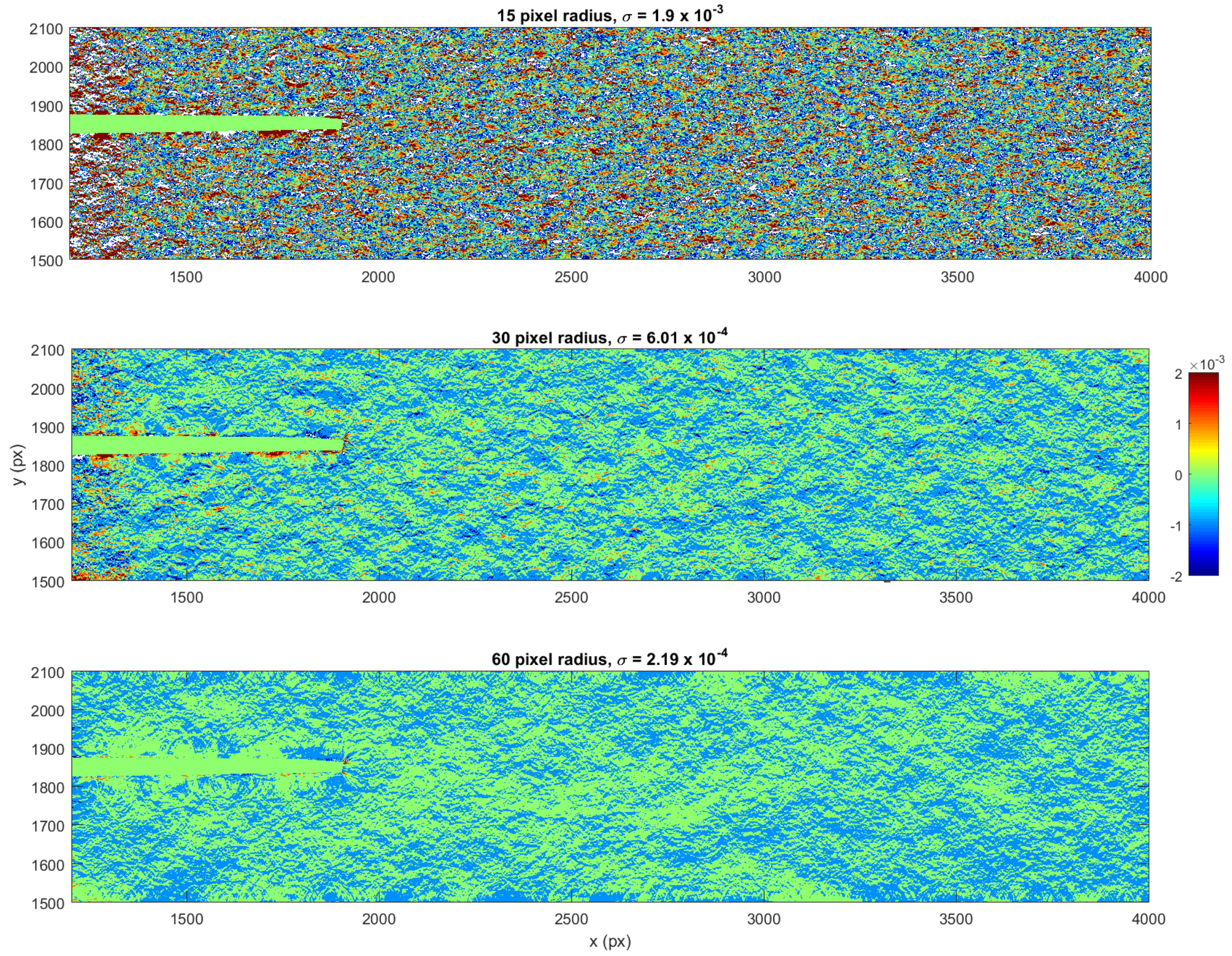

15 pixel radius, $\sigma = 1.9 \times 10^{-3}$

30 pixel radius, $\sigma = 6.01 \times 10^{-4}$

60 pixel radius, $\sigma = 2.19 \times 10^{-4}$

{exx_close_calib.eps}

Figure 2: ε_{xx} calculated from the displacement data shown in Figure 1. Standard deviation of the strain maps are given in the figure headings.

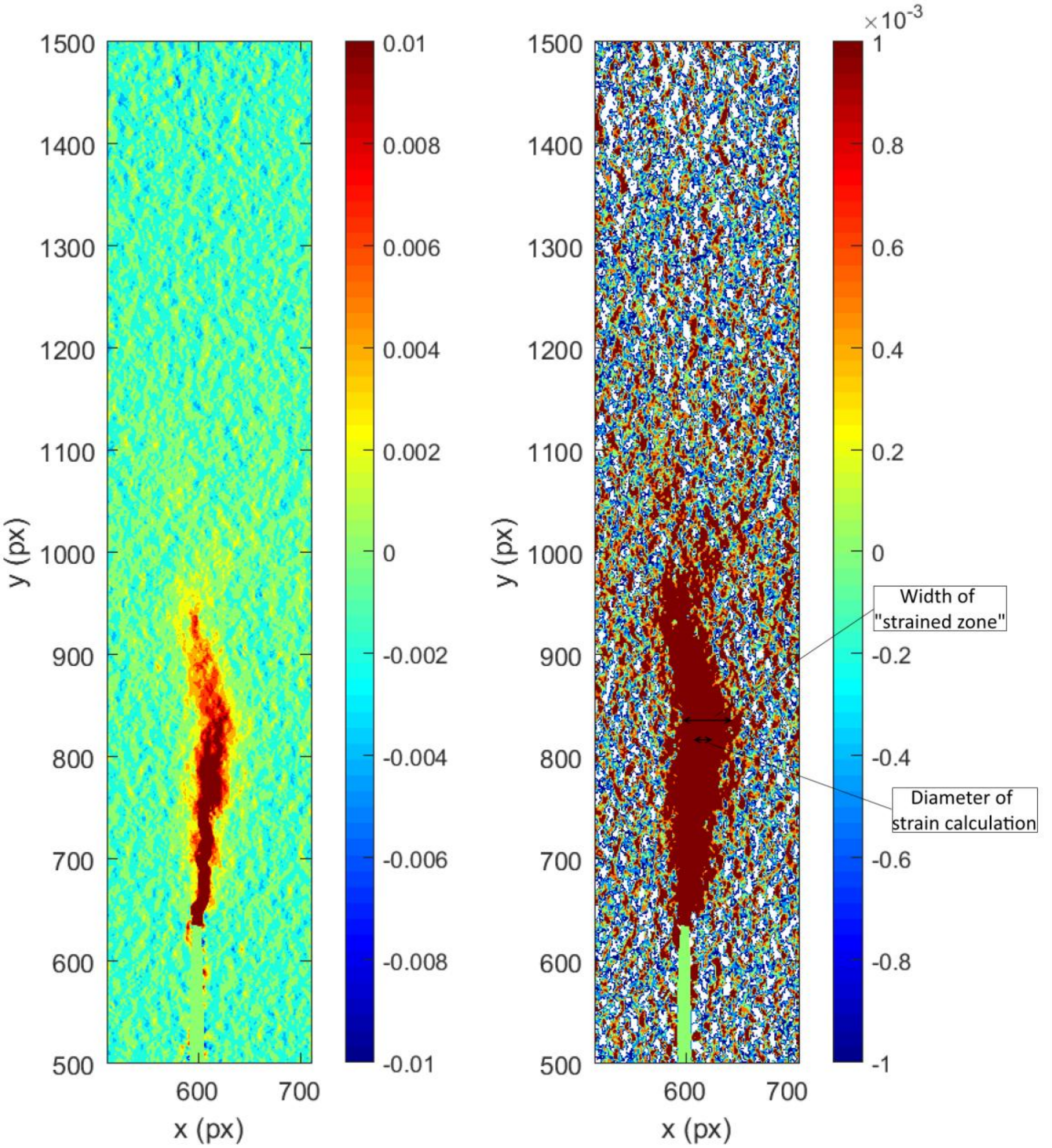

{exx_far_calib2.png}

Figure 3: ε_{xx} for images exhibiting significant process zone development. (Left) shown with a large contour range to highlight the gradation of strain. (Right) Same data shown with a small contour range to highlight the extent of the process zone. It can be seen that the width of apparent process zone exceeds the diameter of the DIC calculation.

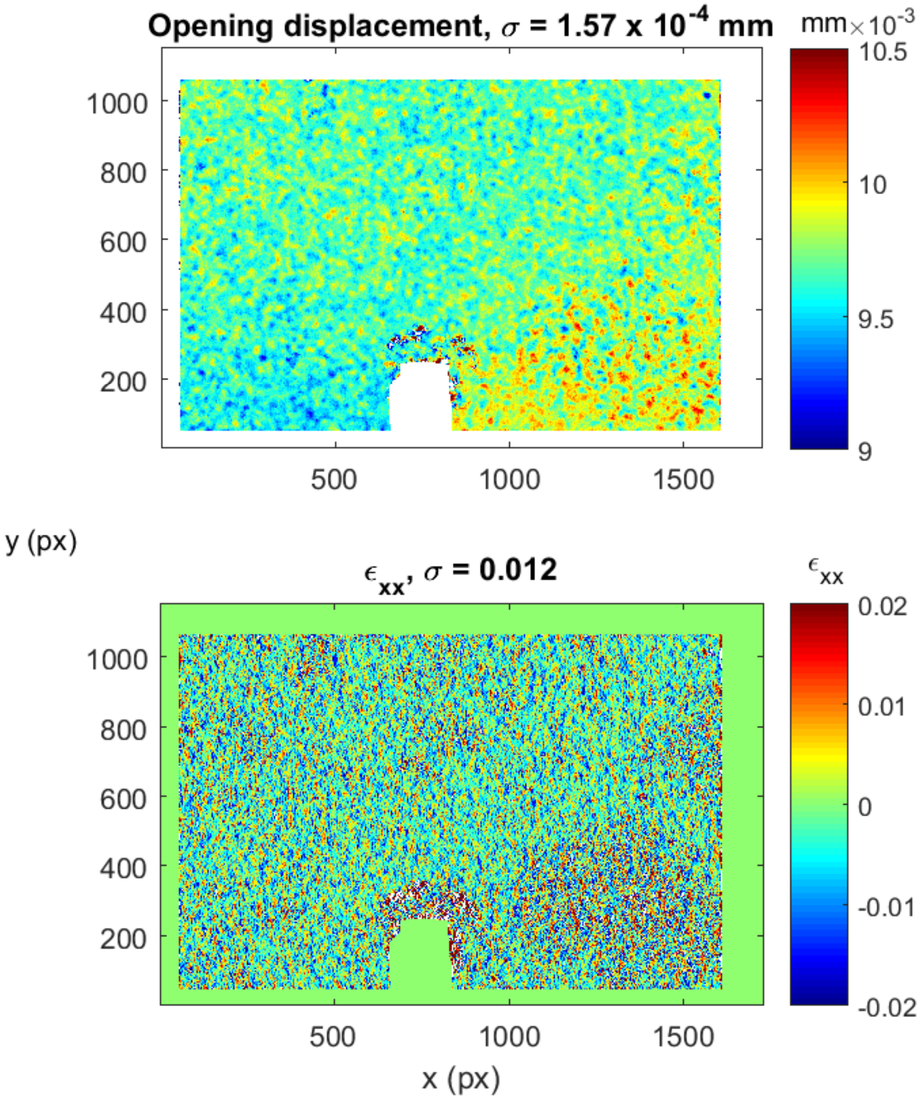

{microDIC_calib.eps}

Figure 4: Opening displacement and ε_{xx} for images taken 2 seconds apart for the micro-camera. Standard deviation of the strain maps are given in the figure headings.

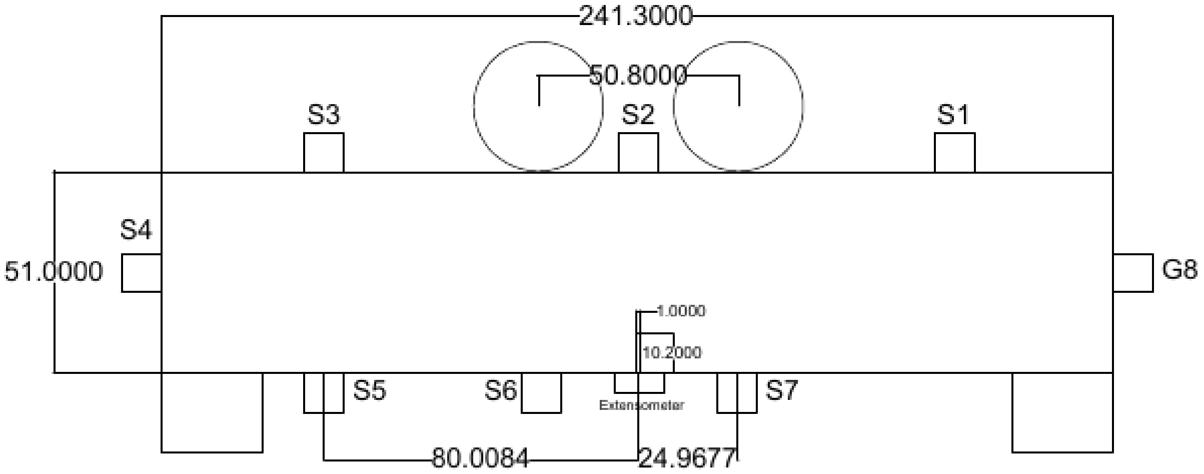

{specDim2.pdf}

Figure 5: Specimen geometry and AE sensor locations. S refers to PAC Micro30S sensors, and G refers to a Glaser-type sensor. Boxes denote locations of the loading platens. Units in mm.

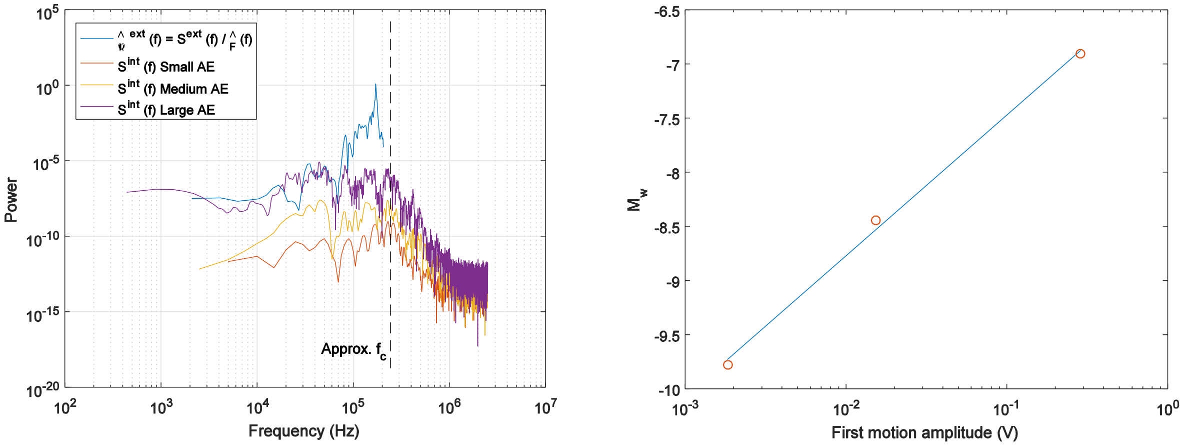

{bd_calib_4.eps}

{mw_amp3.eps}

Figure 6: (a) Spectra of the instrument-apparatus response and three AE events seen during the four point bending experiment. The notation is the same as that used by McLaskey et al. (2015). The AE magnitudes were M_W = -9.78, -8.45 and -6.91. f_c is the corner frequency of the AE events. (b) For these three AE events, a linear relation was found between M_W and its first motion amplitude.

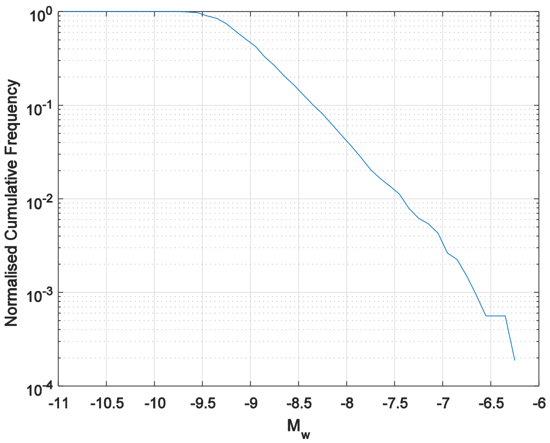

{b-value2.eps}

Figure 7: Magnitude-frequency distribution plot for all events in the four point bending experiment, based on the calibration shown in Figure 2.

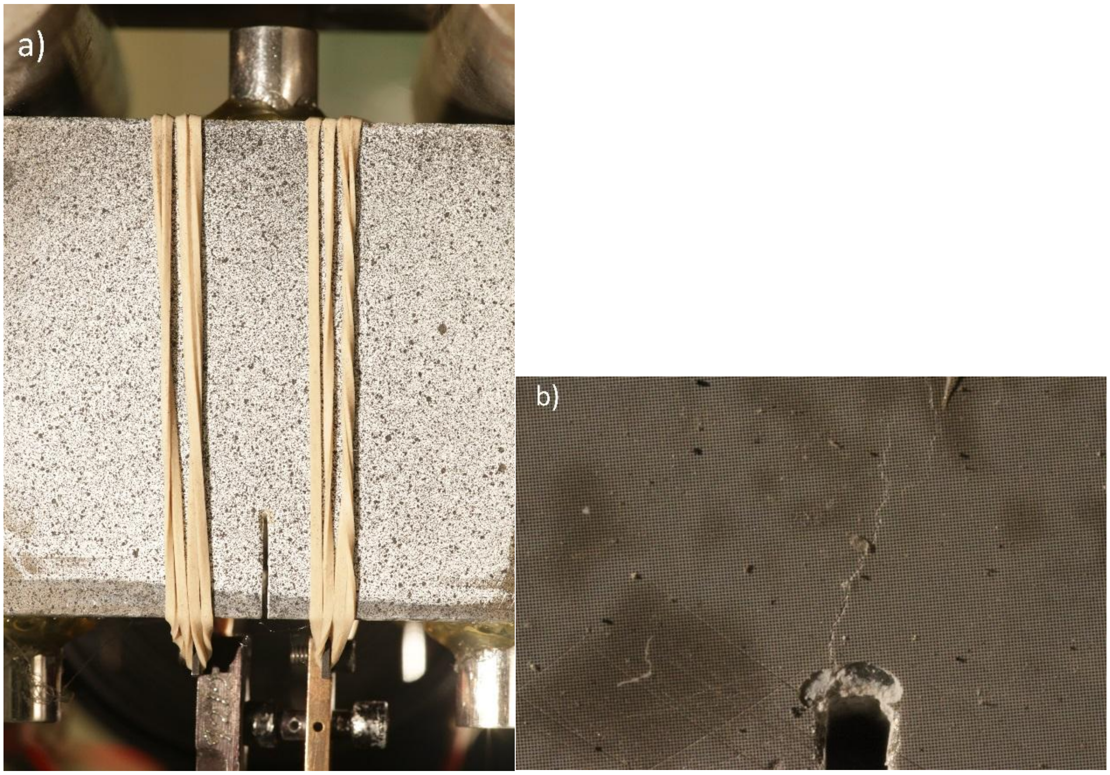

{ HR.jpg} {IMG_7138.jpg}

Figure 8: (a) Reference image for the front camera, corresponding to a field of view (FOV) of around 5 x 7.5 cm. (b) Reference image for the back camera, corresponding to a FOV of around 2.95 x 4.425 mm.

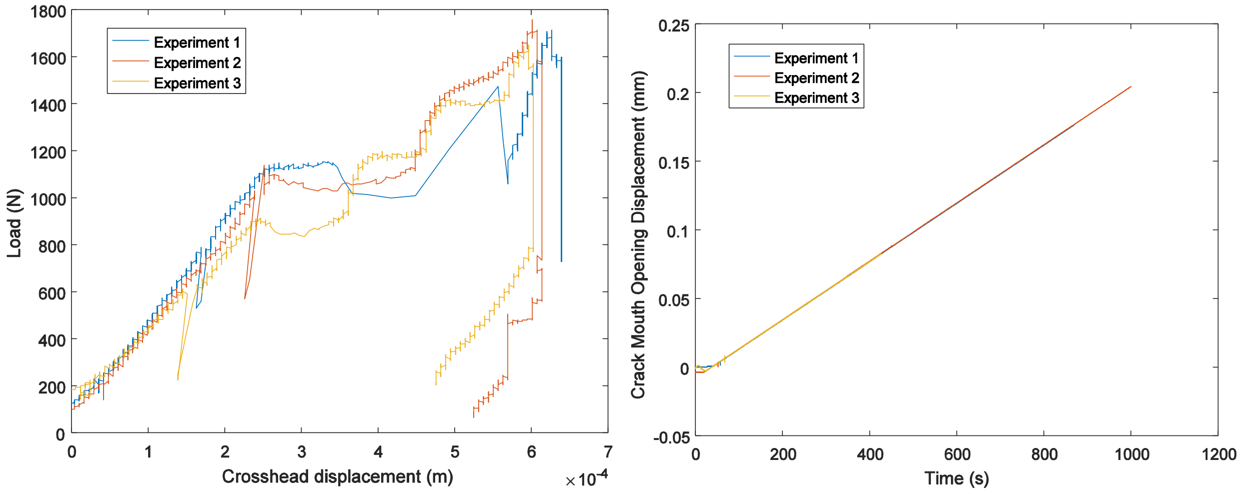

{repeats.eps} {cmod.eps}

Figure 9: (a) Load-displacement data for the three experiments. Drops in load during the initial elastic region are points in time where the loading was paused to refocus the cameras. (b) Crack mouth opening displacement over time for all three experiments, with a nominal rate of 0.0127 mm/min.

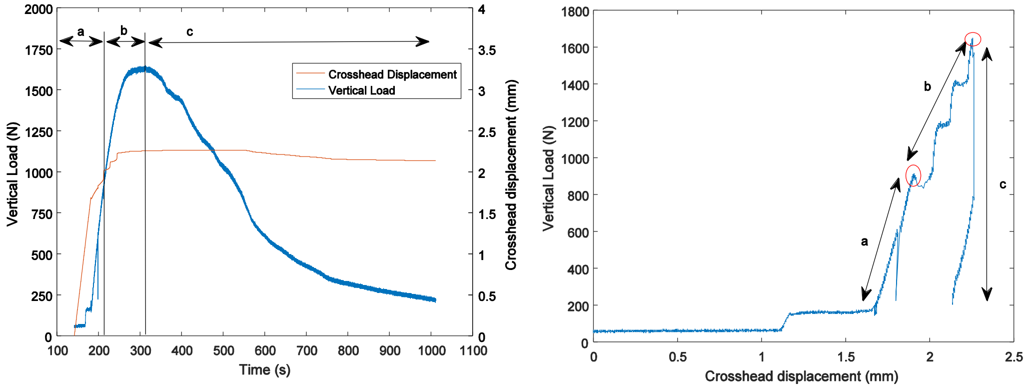

{loadDispSeparate3.eps} {loadDisp4.eps}

Figure 10: (a) Crosshead load and displacement over time. (b) Same data expressed as load-displacement to identify key stages of behaviour: 'a' linear load-displacement behaviour indicating elastic deformation. 'b' Vertical load appears to increase in 3 distinct non-linear steps, indicating the material is no longer deforming elastically. 'c' The load decreases while the crosshead maintains its position, indicating that the fracture is steadily propagating. The transition points are indicated in the red circles.

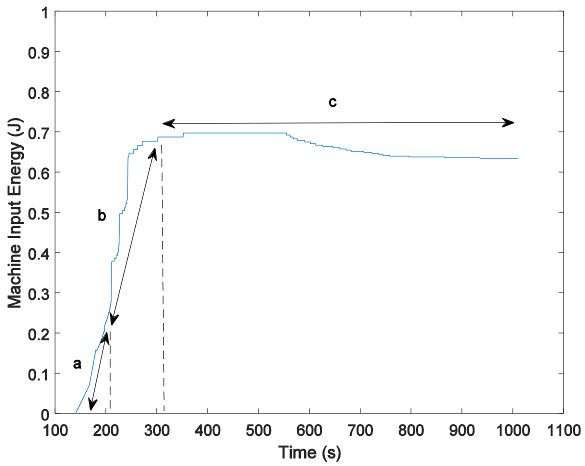

{energyTime2.eps}

Figure 11: Machine input work, calculated from the integral of Figure 6b. The three stages of deformation are also highlighted here. The behaviour transitions from ’a’ to ’b’ at around 210 s, and from ’b’ to ’c’ at around 310 s.

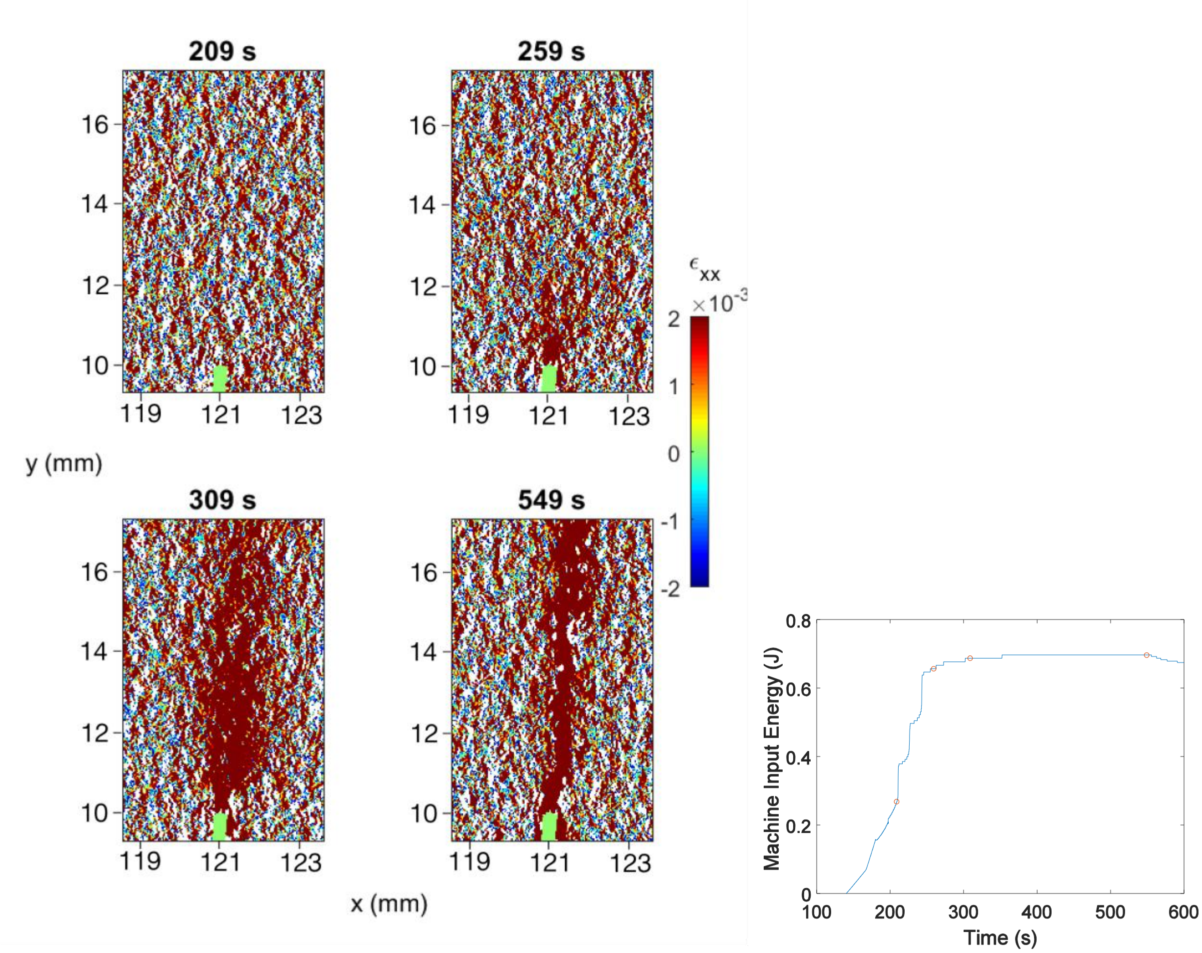

{exx_time3.png}

{exx_time2_times.eps}

Figure 12: (a) Opening strain at key points in time as indicated in Figure 7. (b) Points in time indicated on the energy-time curve.

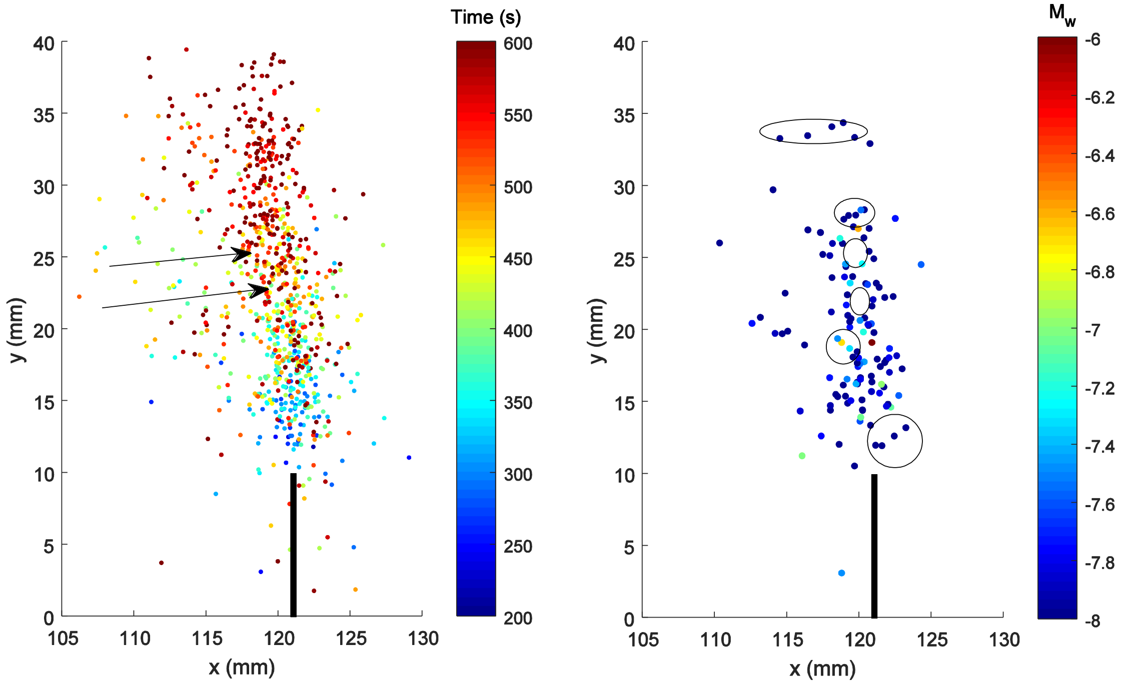

{whole_exp_AE_time4.eps} {whole_exp_AE_mag6.eps}

Figure 13: (a) AE events for entire experiment, coloured by time. Arrow indicates a specific zone in the AE cloud where there appears to be no events. (b) AE events with $M_W > -8.3$, coloured by magnitude. Black circles indicate events occurring along possible grain boundaries or zone of no events.

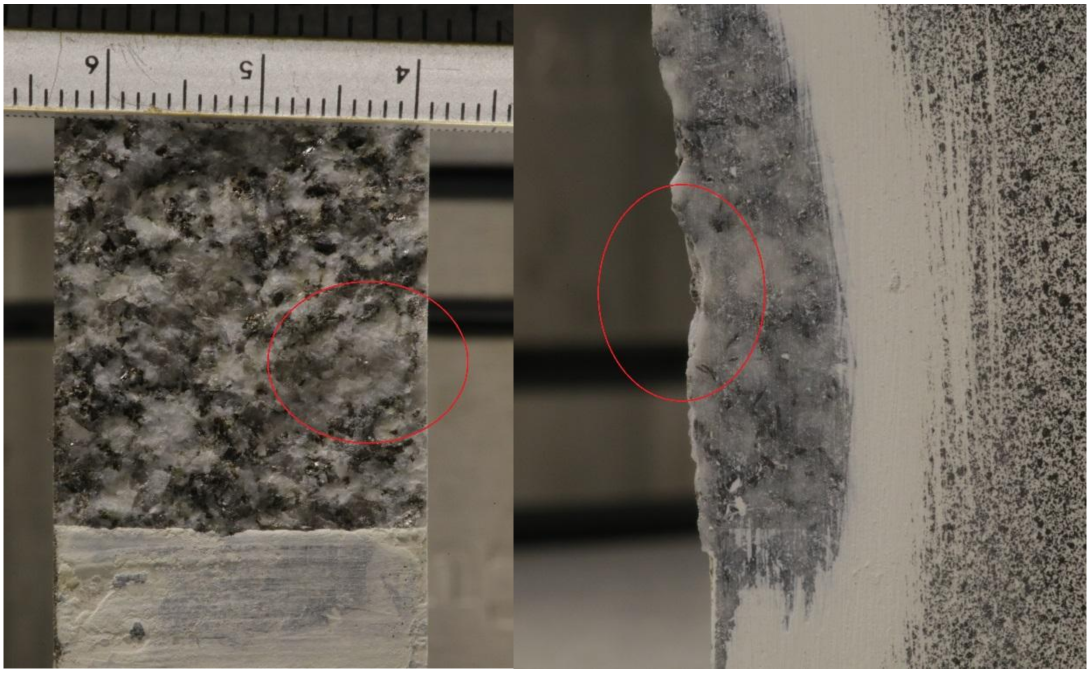

{qzG.jpg}

Figure 14: (a) Detailed photo of the crack surface, large quartz grain shown in red. Scale in cm. White flat surface is the pre-cut notch. (b) Curvature in the crack path due to the quartz grain.

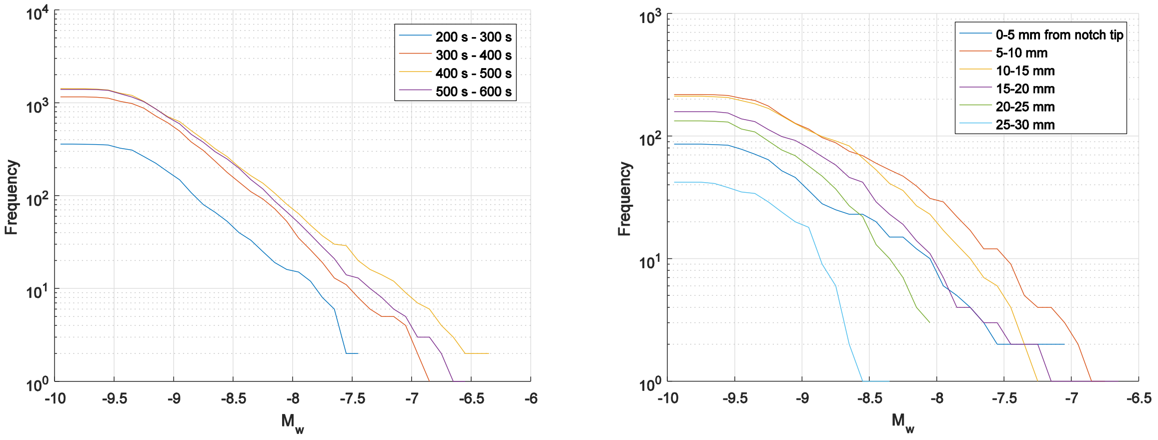

{bV_time.eps}

{bV_dist.eps}

Figure 15: (a) magnitude-frequency distribution of AE events at different time intervals. (b) magnitude-frequency distribution of AE events at different distances from the notch tip.

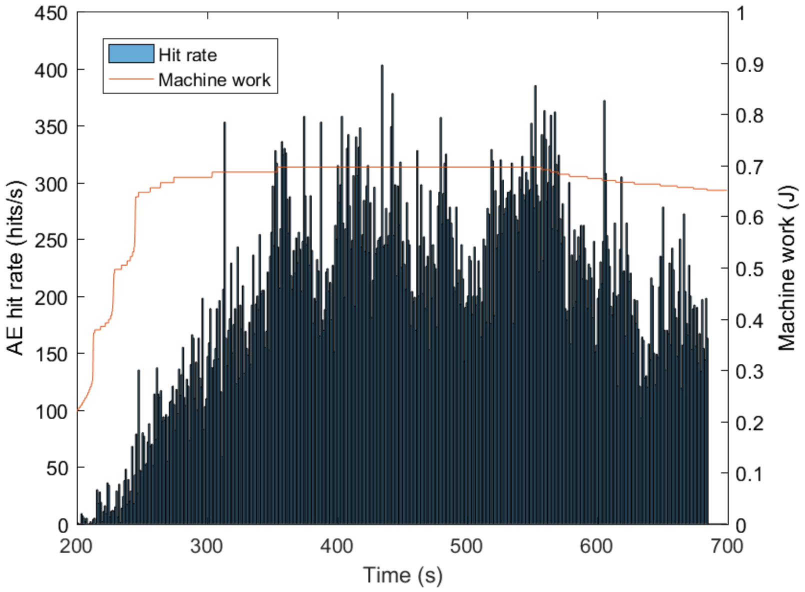

{hitrate2.eps}

Figure 16: AE hit rate over the course of the experiment. Figure 7 is superimposed for reference.

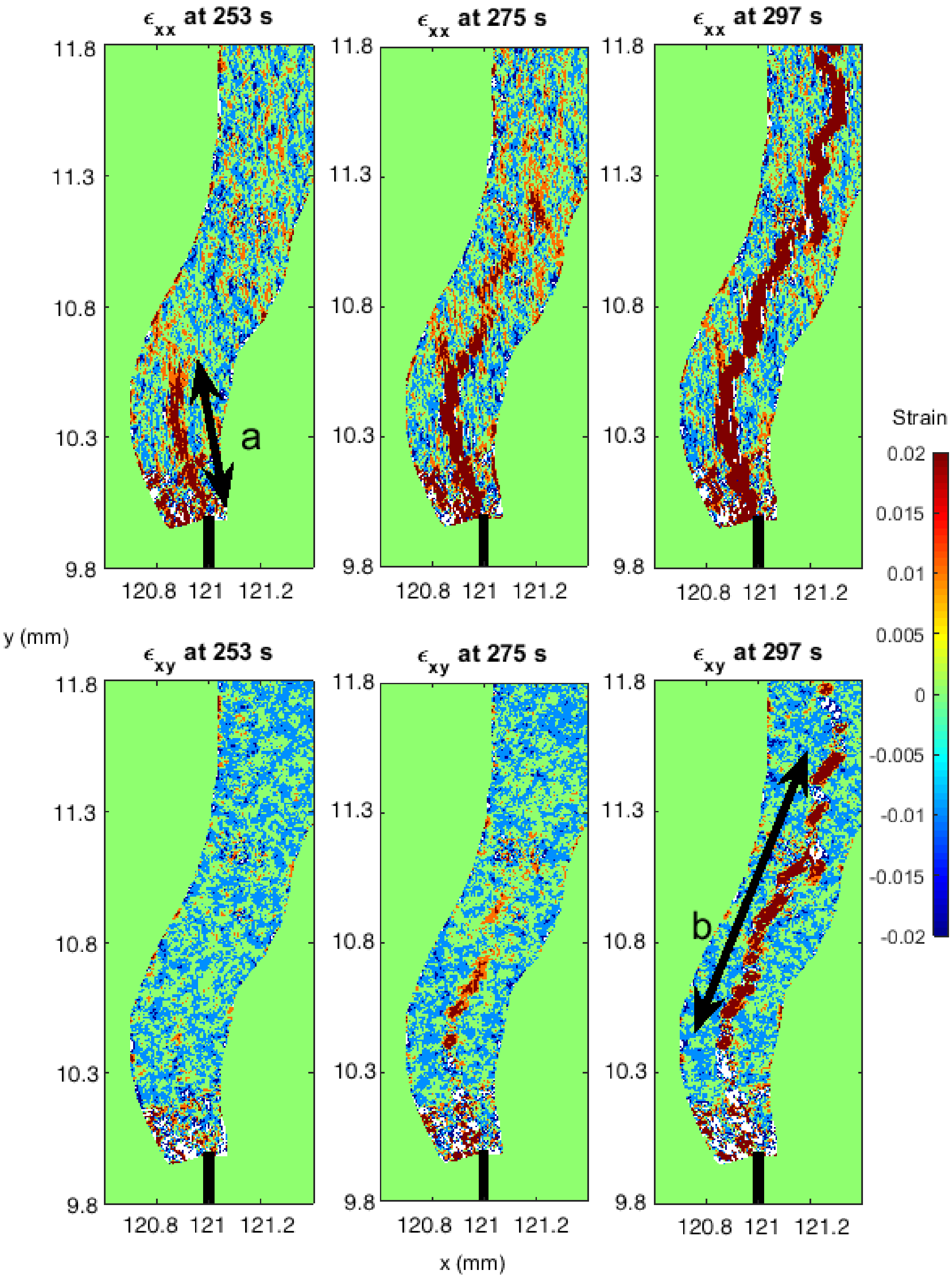

{microstrains4.png}

Figure 17: ε_{xx} and ε_{xy} at 253, 275 and 297 s of the experiment. The times correspond to approximately 90%, 95% and 100% of peak load respectively. The black bar in each figure schematically indicates approximate location of notch tip. Zone a: Initial portion of the crack, which appears to be purely tensile given that ε_{xy} indicates very little strain. Zone b: Ensuing en-echelon crack, which clearly shows step-like structure particularly in the ε_{xy} plot.

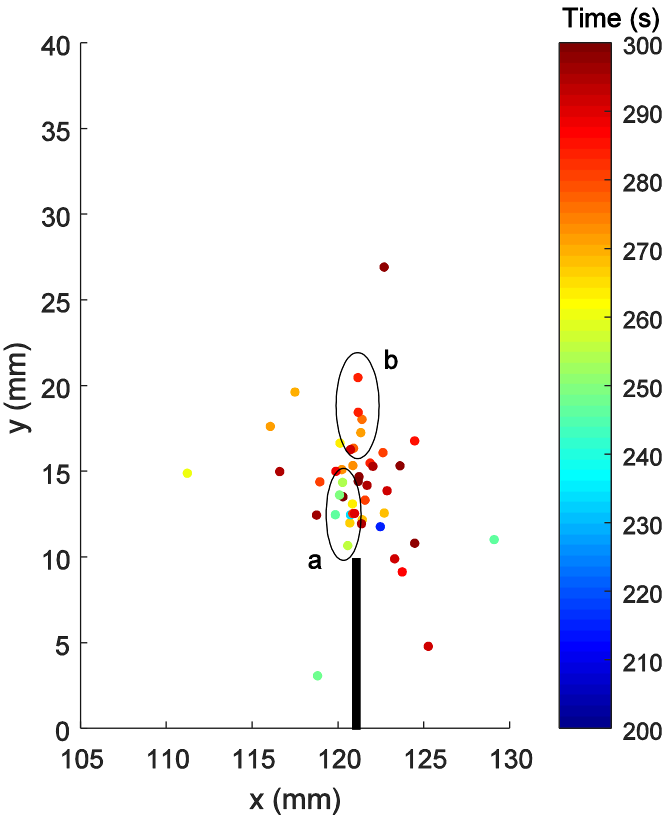

{0-300_2.eps}

Figure 18: Source locations for events occurring between 0 and 300 s in the experiment. Colour shows time of occurrence. Clusters a and b each seem to occur closely in time in a linear pattern.

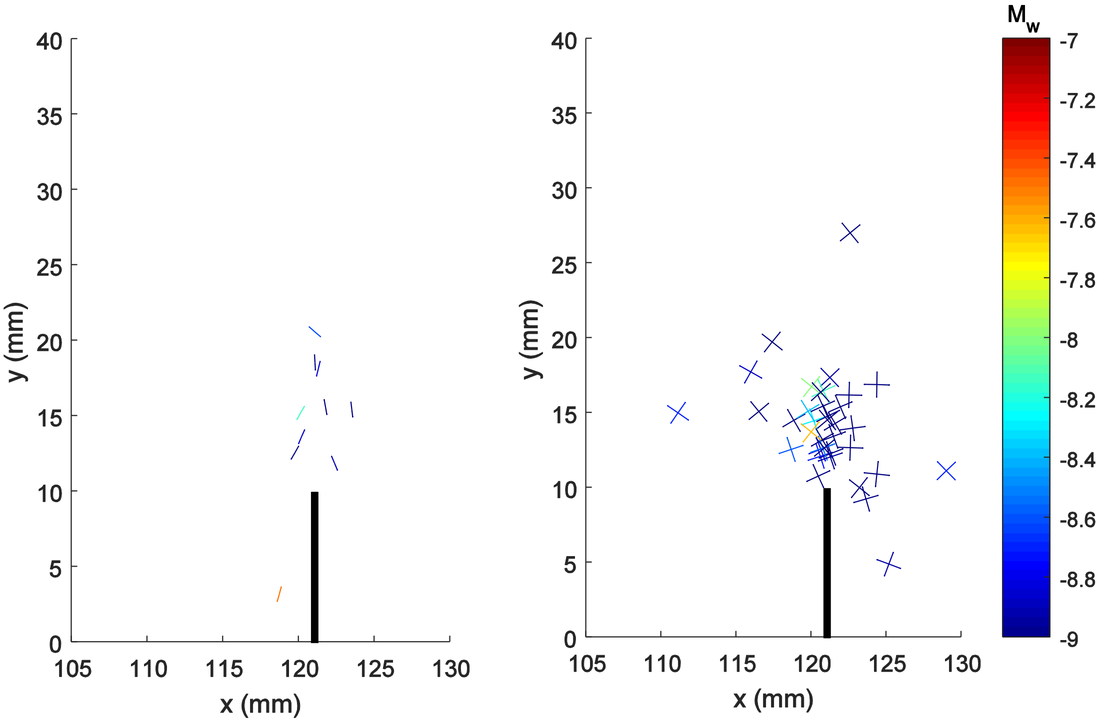

{0-300tensile2.eps}

{0-300shear2.eps}

Figure 19: (a) Microcrack orientation and location for tensile events occurring between 0 and 300 seconds. (b) Orientation and location of shear conjugate planes. Colour indicates magnitude.

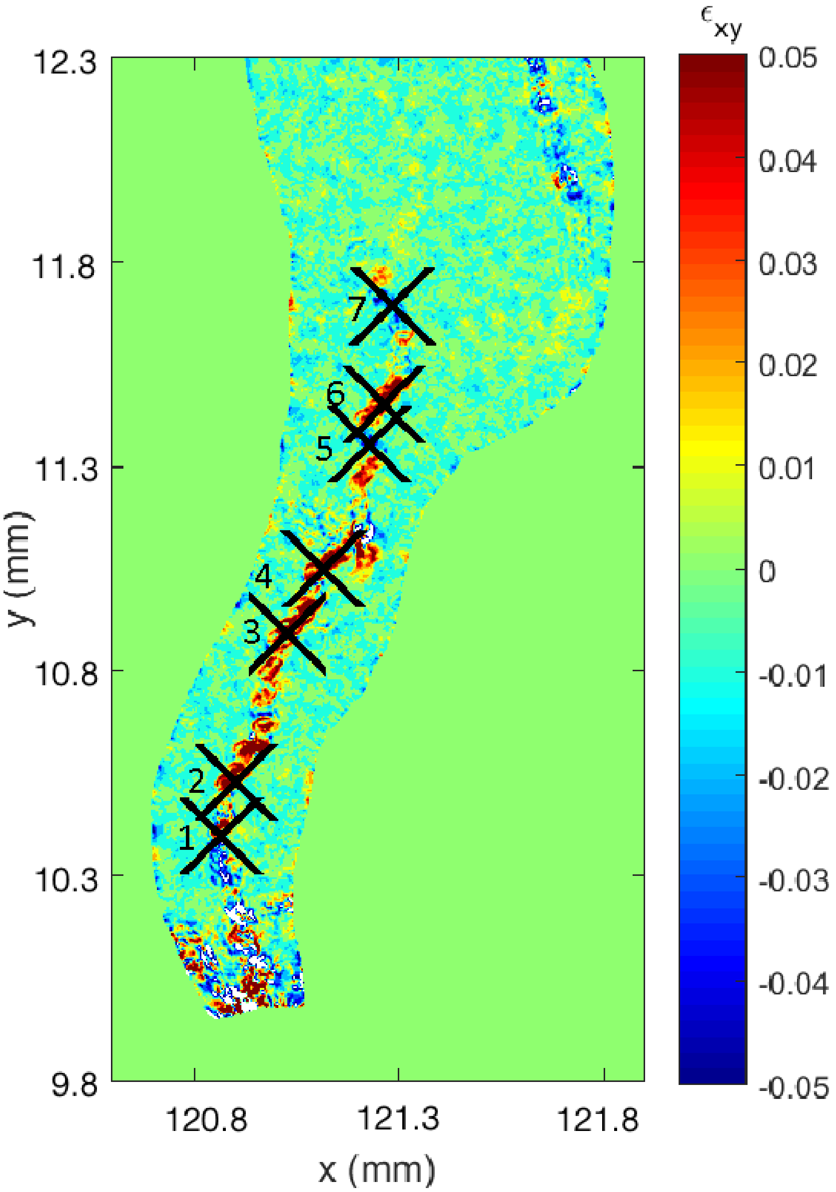

{exy_detailed5.png}

Figure 20: Detailed view of ε_{xy} at 300 s of the experiment. Black crosses indicate query points used for Figure 17. Point 1 is the lowermost point, and point 7 is the uppermost.

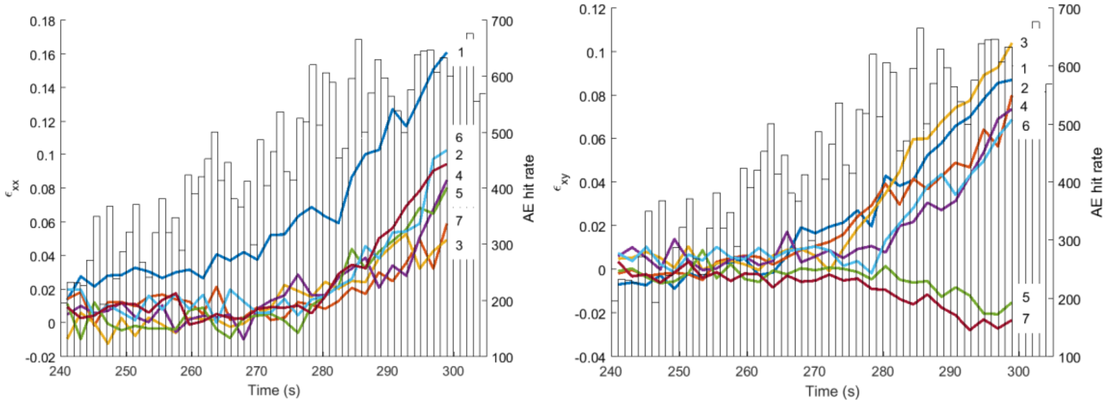

{hitrate_tensilestrain.eps} {hitrate_shearstrain.eps}

Figure 21: Evolution of (a) ε_{xx} and (b) ε_{xy} over time (taken at 2 s intervals) at the query points specified in Figure 16. Query point 1 is the lowest point, and point 7 is the uppermost point. Histogram shows the AE hit rate over the same period.

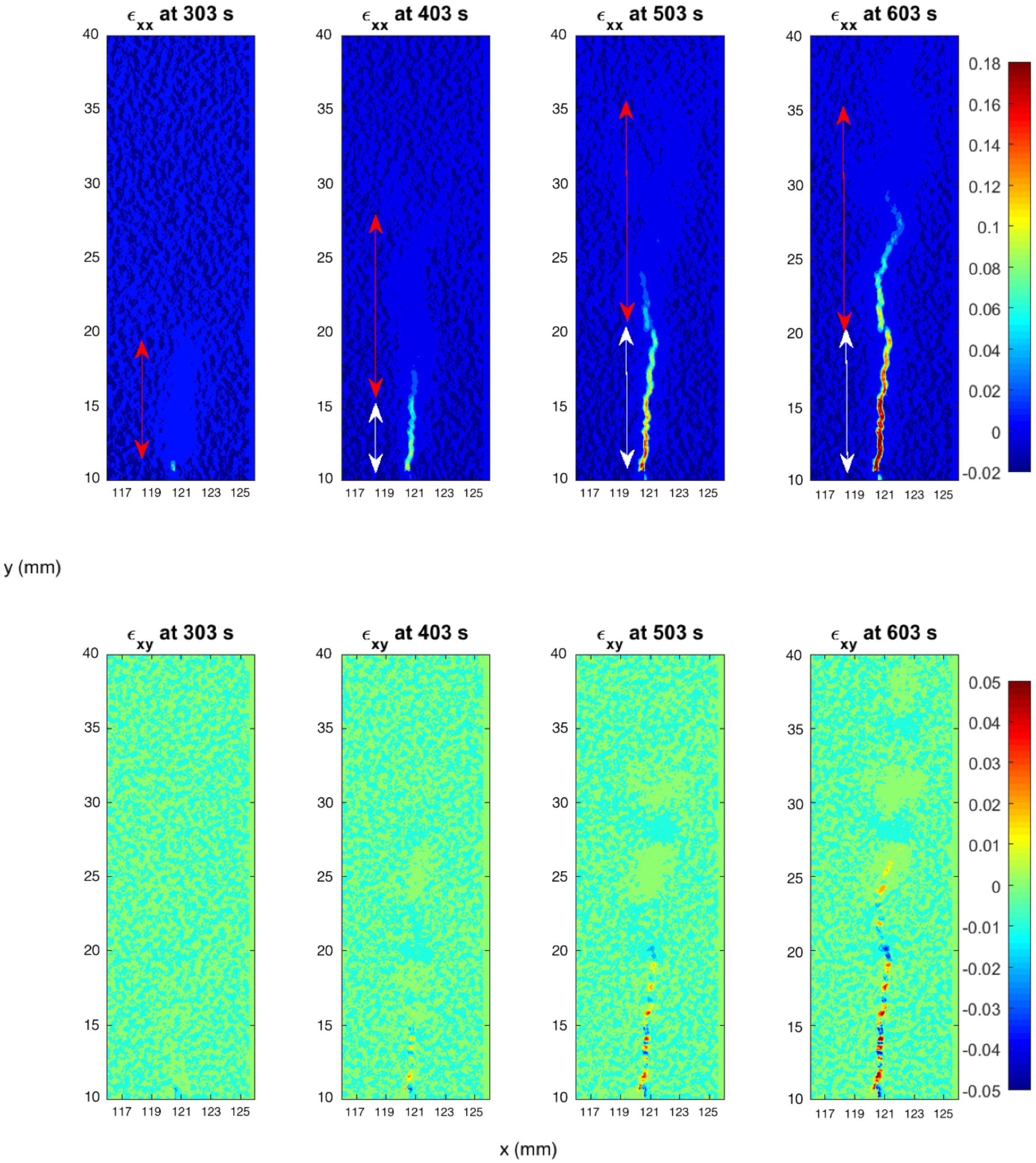

{HR_time2.png}

Figure 22: (a) ε_{xx} and (b) ε_{xy} on the macro-DIC over the course of the experiment. Red and white arrows indicate the best qualitative estimate of the extent of the process zone and crack respectively.

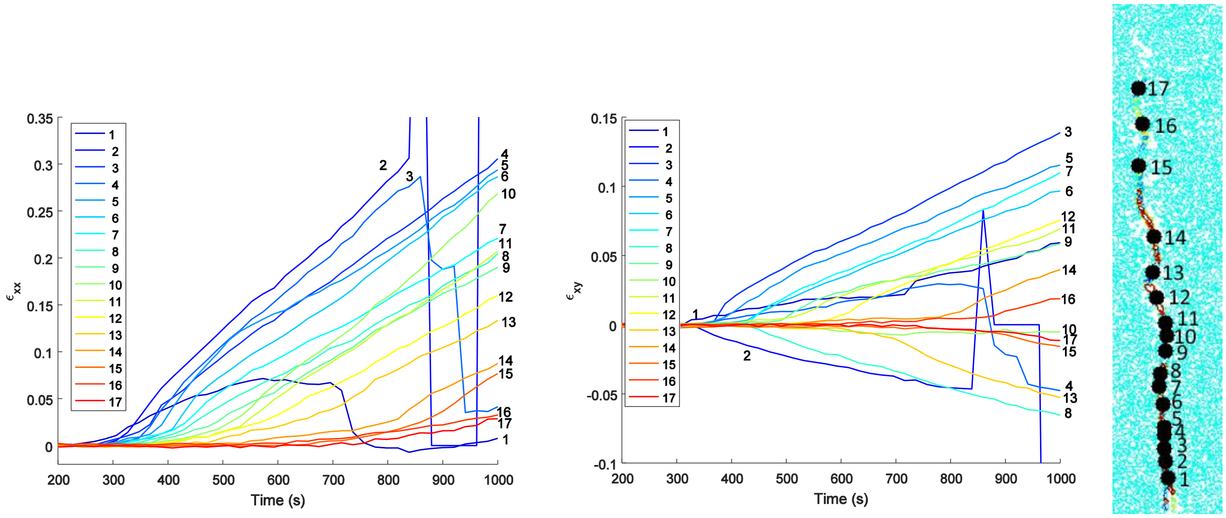

{0-end_T_graph3.eps} {0-end_S_graph3.eps} {Picture1.png}

Figure 23: ε_{xx} and ε_{xy} over time, taken at 20 s intervals. Rightmost image (c) shows locations of query points. The strains at query points 1, 2 and 3 appear to be anomalous towards the end of the experiment, which may be due to very large crack opening since the employed DIC algorithm does not account for discontinuities.

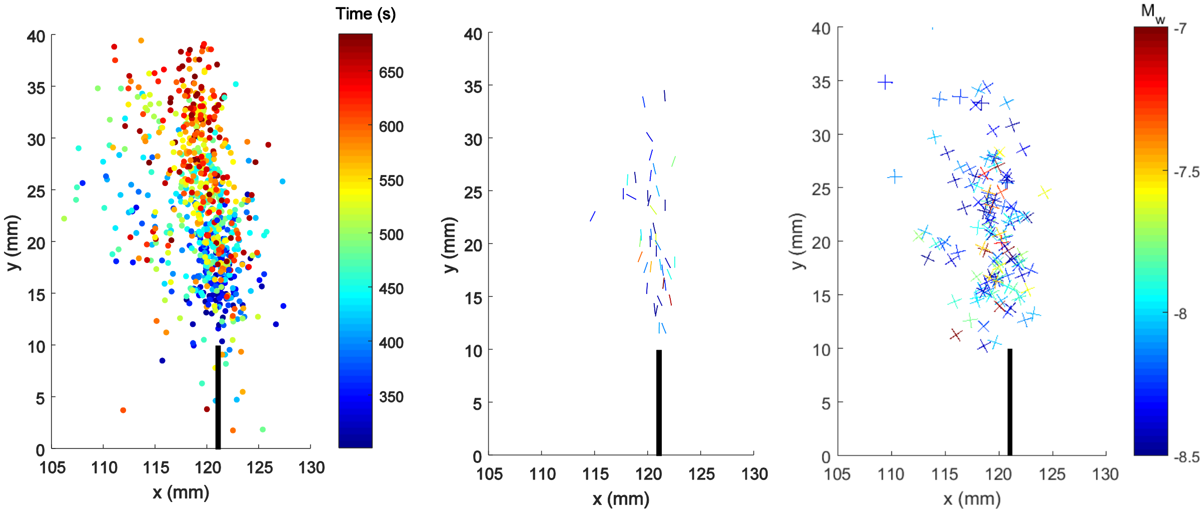

{300-end_AE2.eps} {300-end_tensile.eps} {300-end_shear.eps}

Figure 24: (a) Location of all AE events occurring after 300 s. (b) Microcrack orientation and location for tensile events with M_w > -8:5. (c) Orientation and location of shear conjugate planes. Colour indicates magnitude.

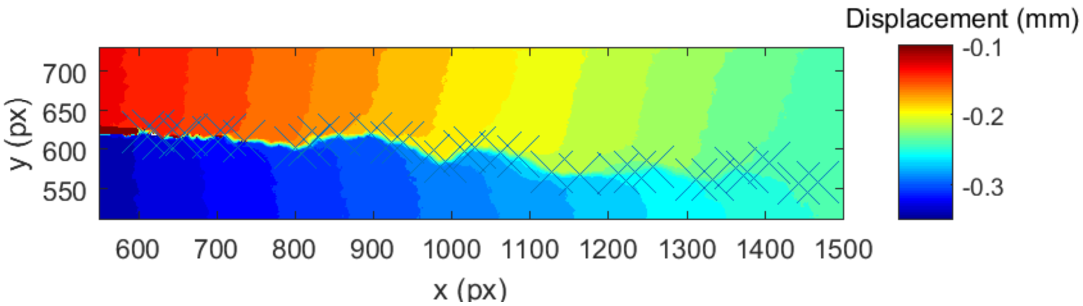

{lotsQuery.eps}

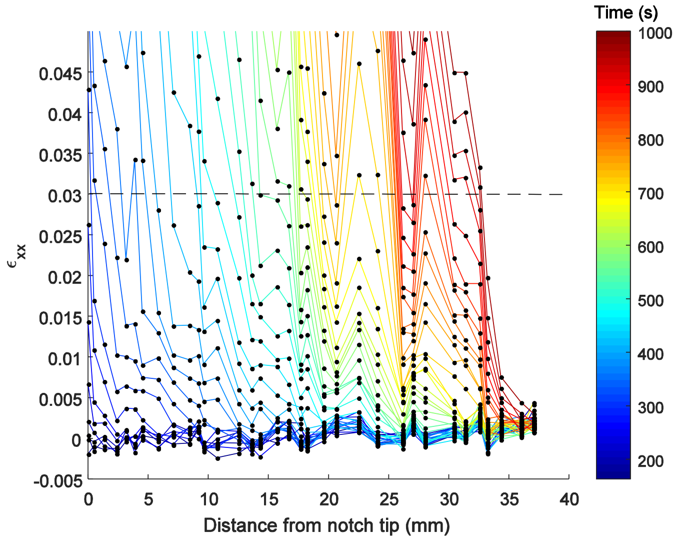

{p_c_calib.eps}

Figure 25: (a) Displacement contour plot at 1000 s showing query points chosen based on an iso-displacement contour that best estimated the location of the crack. (b) Strain data (y-axis) shown as a function of distance from notch tip on the x-axis and time in the colour scheme. Dotted line at y = 0.03 shows the calibrated strain value, which was used to calculate the crack extent.

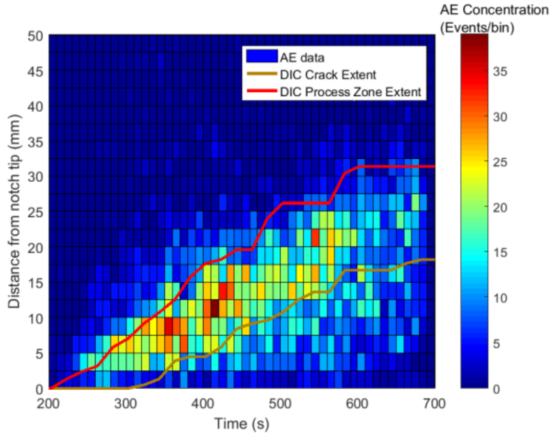

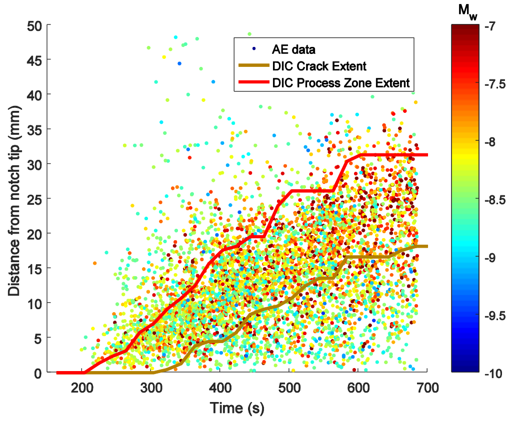

{extent_AE_conc4.eps}

{extent_AE_mag4.eps}

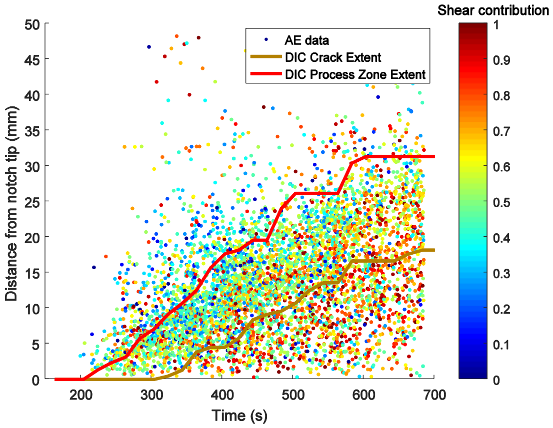

{extent_AE_shear4.eps}

Figure 26: Distance from the notch tip for AE events, DIC process zone (red line) and DIC crack extent (brown line). Left image shows the density of the location of AE events as binned in the figure. Middle image is coloured by magnitude, right image by contribution of shear ratio as per the moment tensor decomposition, where 0 indicates no shear and 1 indicates a pure double-couple mechanism.